Swarthmore College

Works

Physics & Astronomy Faculty Works

Physics & Astronomy

7-11-2010

A Mass-Loss Rate Determination For Zeta Puppis From The Quantitative Analysis Of X-Ray Emission-Line Profiles

David H. Cohen
Swarthmore College, dcohen1@swarthmore.edu

M. A. Leutenegger

Emma Edwina Wollman , '09

J. Zsargó

D. J. Hillier

See next page for additional authors

Authors

David H. Cohen; M. A. Leutenegger; Emma Edwina Wollman , '09; J. Zsargó; D. J. Hillier; R. H.D. Townsend; and S. P. Owocki

A mass-loss rate determination for ζ Puppis from the quantitative analysis of X-ray emission-line profiles

David H. Cohen,[1][*] Maurice A. Leutenegger,[2] Emma E. Wollman,[1,3] Janos Zsargó,[4,5] D. John Hillier,[4] Richard H. D. Townsend[6,7] and Stanley P. Owocki[6]

[1]*Swarthmore College, Department of Physics and Astronomy, Swarthmore, PA 19081, USA*
[2]*NASA/Goddard Space Flight Center, Laboratory for High Energy Astrophysics, Code 622, Greenbelt, MA 20771, USA*
[3]*California Institute of Technology, Department of Physics, Pasadena, CA 91125, USA*
[4]*University of Pittsburgh, Department of Physics and Astronomy, 3941 O'Hara Street, Pittsburgh, PA 15260, USA*
[5]*Instituto Politécnico Nacional, Escuela Superior de Física y Matemáticas, C.P. 07738, Mexico, D.F., Mexico*
[6]*University of Delaware, Bartol Research Institute, Newark, DE 19716, USA*
[7]*University of Wisconsin, Department of Astronomy, Madison, 475 N. Charter Street, Madison, WI 53706, USA*

ABSTRACT

We fit every emission line in the high-resolution *Chandra* grating spectrum of ζ Pup with an empirical line profile model that accounts for the effects of Doppler broadening and attenuation by the bulk wind. For each of 16 lines or line complexes that can be reliably measured, we determine a best-fitting fiducial optical depth, $\tau_* \equiv \kappa \dot{M}/4\pi R_* v_\infty$, and place confidence limits on this parameter. These 16 lines include seven that have not previously been reported on in the literature. The extended wavelength range of these lines allows us to infer, for the first time, a clear increase in τ_* with line wavelength, as expected from the wavelength increase of bound–free absorption opacity. The small overall values of τ_*, reflected in the rather modest asymmetry in the line profiles, can moreover all be fitted simultaneously by simply assuming a moderate mass-loss rate of $3.5 \pm 0.3 \times 10^{-6}\,\mathrm{M_\odot\,yr^{-1}}$, without any need to invoke porosity effects in the wind. The quoted uncertainty is statistical, but the largest source of uncertainty in the derived mass-loss rate is due to the uncertainty in the elemental abundances of ζ Pup, which affects the continuum opacity of the wind, and which we estimate to be a factor of 2. Even so, the mass-loss rate we find is significantly below the most recent smooth-wind Hα mass-loss rate determinations for ζ Pup, but is in line with newer determinations that account for small-scale wind clumping. If ζ Pup is representative of other massive stars, these results will have important implications for stellar and Galactic evolution.

Key words: radiative transfer – stars: early-type – stars: individual: ζ Pup – stars: mass-loss – stars: winds, outflows – X-rays: stars.

1 INTRODUCTION

Massive stars can lose a significant fraction of their original mass during their short lifetimes due to their strong, radiation-driven stellar winds. Accurate determinations of these stars' mass-loss rates are therefore important from an evolutionary point of view, as well as for understanding the radiative driving process itself. Massive star winds are also an important source of energy, momentum and (chemically enriched) matter deposition into the interstellar medium, making accurate mass-loss rate determinations important from a Galactic perspective.

A consensus appeared to be reached by the late 1990s that the mass-loss rates of O stars were accurately known observationally and theoretically, using the modified (Pauldrach, Puls & Kudritzki 1986) CAK (Castor, Abbott & Klein 1975) theory of line-driven stellar winds. This understanding was thought to be good enough that ultraviolet (UV) observations of spectral signatures of their winds could be used to determine their luminosities with sufficient accuracy to make extragalactic O stars standard candles (Puls et al. 1996).

This consensus has unravelled in the last few years, mostly from the observational side, where a growing appreciation of wind clumping – an effect whose importance has long been recognized (Eversberg, Lepine & Moffat 1998; Hamann & Koesterke 1999; Hillier & Miller 1999) – has led to a re-evaluation of mass-loss rate diagnostics, including Hα emission, radio and infrared (IR)

[*]E-mail: cohen@astro.swarthmore.edu

free–free emission and UV absorption (Bouret, Lanz & Hillier 2005; Fullerton, Massa & Prinja 2006; Puls et al. 2006). Accounting for small-scale clumping that affects density squared emission diagnostics – and also ionization balance and thus ionic column density diagnostics like UV resonance lines – leads to a downward revision of mass-loss rates by a factor of several, with a fair amount of controversy over the actual factor (Hamann, Feldmeier & Oskinova 2008; Puls, Vink & Najarro 2008).

X-ray emission-line profile analysis provides a good and independent way to measure the mass-loss rates of O stars. Like the UV absorption-line diagnostics, X-ray emission profile diagnostics are sensitive to the wind column density and thus are not directly affected by clumping in the way density-squared diagnostics are. Unlike the UV absorption-line diagnostics, however, X-ray profile analysis is not very sensitive to the ionization balance; moreover, as it relies on continuum opacity rather than line opacity, it is not subject to the uncertainty associated with saturated absorption lines that hamper the interpretation of the UV diagnostics.

In this paper, we apply a quantitative line profile analysis to the *Chandra* grating spectrum of the early O supergiant, ζ Pup, one of the nearest O stars to the Earth and a star that has long been used as a canonical example of an early O star with a strong radiation-driven wind. Previous analysis of the same *Chandra* data has established that the kinematics of the X-ray-emitting plasma, as diagnosed by the linewidths, are in good agreement with wind-shock theory, and that there are modest signatures of attenuation of the X-rays by the dominant cold wind component in which the shock-heated X-ray-emitting plasma is embedded (Kramer, Cohen & Owocki 2003).

The work presented here goes beyond the profile analysis reported in that paper in several respects. We analyse many lines left out of the original study that are weak, but which carry a significant amount of information. We better account for line blends and are careful to exclude those lines where blending cannot be adequately modelled. We model the continuum emission underlying each line separately from the line itself. We use a realistic model of the spectrometers' responses and the telescope and detector effective area. And we include the high-energy grating (HEG) spectral data, where appropriate, to augment the higher signal-to-noise ratio medium energy grating (MEG) data that Kramer et al. (2003) reported on.

Implementing all of these improvements enables us to derive highly reliable values of the fiducial wind optical depth parameter, $\tau_* \equiv \kappa \dot{M}/4\pi R_* v_\infty$, for each of 16 emission lines or line complexes in the *Chandra* grating spectrum of ζ Pup. Using a model of the wavelength-dependent wind opacity, κ, and values for the star's radius, R_*, and wind terminal velocity, v_∞, derived from UV and optical observations, we can fit a value of the mass-loss rate, $\dot{M}$, to the ensemble of τ_* values, and thereby determine the mass-loss rate of ζ Pup based on the observed X-ray emission-line profiles.

In doing this, we also can verify that the wavelength dependence of the optical depth values – derived separately for each individual line – is consistent with that of the atomic opacity of the bulk wind, rather than the grey opacity that would, for example, be obtained from an extremely porous wind (Oskinova, Feldmeier & Hamann 2006; Owocki & Cohen 2006). While a moderate porosity might reduce somewhat the effective absorption while still retaining some wavelength dependence, for simplicity our analysis here assumes a purely atomic opacity set by photoelectric absorption, with no reduction from porosity. This assumption is justified by the large porosity lengths required for any appreciable porosity effect on line profile shapes (Owocki & Cohen 2006) and the very small-scale clumping in state-of-the-art two-dimensional radiation hydrodynamics simulations (Dessart & Owocki 2003). Furthermore,

preliminary results indicate that profile models that explicitly include porosity are not favoured over ones that do not (Cohen, Leutenegger & Townsend 2008). We will extend this result in a forthcoming paper but do not address the effect of porosity on individual line profile shapes directly in this paper.

The paper is organized as follows. We begin by describing the *Chandra* data set and defining a sample of well-behaved emission lines for our analysis in Section 2. We briefly evaluate the stellar and wind properties of ζ Pup in Section 3. In Section 4 we describe the empirical profile model for X-ray emission lines and report on the fits to the 16 usable lines and line complexes in the spectrum. We discuss the implications of the profile model fitting results in Section 5, and summarize our conclusions in Section 6.

2 THE *Chandra* GRATING SPECTRUM

All the data we use in this paper were taken on 2000 March 28–29 in a single, 68-ks observation using the *Chandra* High-Energy Transmission Grating Spectrometer (HETGS) in conjunction with the Advanced CCD Imaging Spectrometer (ACIS) detector in spectroscopy mode (Canizares et al. 2005). This is a photon-counting instrument with an extremely low background and high spatial resolution ($\approx$1 arcsec). The first-order grating spectra we analysed have a total of 21 684 counts, the vast majority of which are in emission lines, as can be seen in Fig. 1. We modelled every line or line complex – 21 in total – as we describe in Section 4, and indicate in this figure which of the lines we deemed to be reliable. We only include lines in our analysis that are not so weak or severely blended that interesting parameters of the line profile model cannot be reliably constrained. (See Section 4.2.3 for a discussion of the excluded line blends.)

The HETGS assembly has two grating arrays – the MEG and the HEG – with full width half-maximum (FWHM) spectral resolutions of 0.0023 and 0.0012 Å, respectively. This corresponds to a resolving power of $\mathcal{R} \approx 1000$, or a velocity of $300\,\mathrm{km\,s^{-1}}$, at the longer wavelength end of each grating. The wind-broadened X-ray lines of ζ Pup are observed to have $v_{\mathrm{FWHM}} \approx 2000\,\mathrm{km\,s^{-1}}$, and so are very well resolved by *Chandra*. The wavelength calibration of the HETGS is accurate to $50\,\mathrm{km\,s^{-1}}$ (Marshall, Dewey & Ishibashi 2004).

The two gratings, detector and telescope assembly have significant response from roughly 2 to 30 Å, with typical effective areas of tens of cm^2, which are a strong function of wavelength. In practice, the shortest wavelength line with significant flux in the relatively soft X-ray spectra of O stars like ζ Pup is the S xv line complex near 5 Å, and the longest wavelength feature is the N vii Lyα and N vi Heβ line blend at 24.781 and 24.890 Å. The HEG response is negligible for lines with wavelengths longer than about 16 Å.

The X-ray spectrum of ζ Pup consists of emission lines from H-like and He-like ionization stages of N, O, Ne, Mg, Si and S, and numerous L-shell lines of iron, primarily Fe xvii. The Lyα lines and often the β and even γ lines of the Lyman series are seen for the H-like ions. There is a weak bremsstrahlung continuum beneath these lines. Overall, the spectrum is consistent with an optically thin, thermal plasma in ionization equilibrium with a range of temperatures from one to several million degrees present. It is possible that there are deviations from equilibrium, although the spectrum is not of high enough quality to show this. There is some evidence from the *XMM–Newton* RGS spectrum that a few of the emission lines are optically thick (Leutenegger et al. 2007); a possibility we will take into account when discussing the results for those lines.
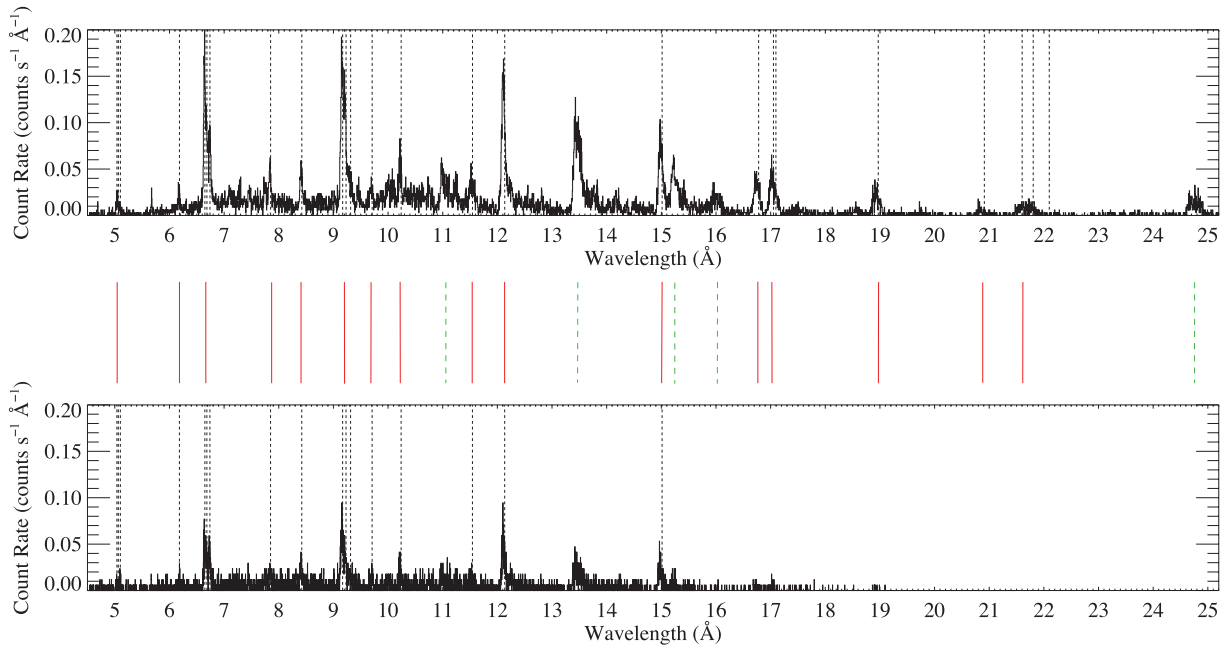
Figure 1. The entire usable portions of the MEG (top) and HEG (bottom) first-order (negative and positive orders co-added) spectra of ζ Pup. The binning is native (5 mÅ for the MEG and 2.5 mÅ for the HEG). Vertical dashed lines in the data panels themselves represent the laboratory rest wavelengths of all the 21 lines and line complexes we fit with the profile model. Solid (red in on-line version) vertical lines between the two spectral plots indicate the lines we successfully fit with profile models and lines we attempted to fit but which were too blended to extract meaningful model parameters are indicated by dashed (green in on-line version) lines. For all blended emission lines we show only one of these solid or dashed lines between the panels, and align it with the bluest line in the blend.

3 THE STAR

ζ Puppis is a relatively nearby, bright and well-studied early O supergiant (O4 If) that shows the enhanced nitrogen and deficient carbon and oxygen that is indicative of CNO cycle processed material. Helium is also overabundant (Puls et al. 2006). The star's rapid rotation may explain the photospheric abundances, though they may instead have resulted from the supernova explosion that is invoked to explain its high space velocity (Vanbeveren, de Loore & van Rensbergen 1998). On the other hand, no special mechanism may need to be invoked if the lifetime of mass-loss of ζ Pup has removed enough of the star's envelope to expose nuclear processed material.

There is some uncertainty regarding the distance to ζ Pup. The spectroscopic parallax (Markova et al. 2004) and trigonometric parallax (Perryman et al. 1997) are in good agreement (∼460 and 429^{+120}_{-77} pc, respectively). But it has also been suggested that ζ Pup lies farther away, at $d \approx 730$ pc, where its space motion and age are consistent with an origin in the Vela Molecular Ridge (Sahu 1992; Sahu & Blaauw 1993). This larger distance implies a larger radius and an Hα mass-loss rate that is larger by a factor of 2. On the other hand, the *Hipparcos* data have recently been reanalysed and a smaller distance – 332 pc – has been found (van Leeuwen 2007).

We stress that the adopted distance does not affect the X-ray line profile fitting results directly. But it does affect the mass-loss rate we derive from our fits via the dependence of $\dot{M}$ on R_*, and it affects the fiducial mass-loss rate to which we compare the value we derive from the X-ray profiles in this paper. The Hα and radio mass-loss rates scale as $\dot{M} \propto d^{1.5}$ and the mass-loss rate we derive from the profile fitting results scales as $\dot{M} \propto d$, so the ratio scales only as the square root of the distance. Thus, any change in the distance

will not strongly affect the discrepancy we find between the fiducial mass-loss rate and the one we derive from the X-ray line profiles. The radius we use for our mass-loss rate calculation in this paper assumes the spectroscopic parallax distance of 460 pc, which is also assumed for the fiducial Hα mass-loss rate determination.

Detailed spectral synthesis has been carried out from the UV to the IR to determine the stellar and wind properties of ζ Pup, which we list in Table 1. Most of these parameters are taken from Puls et al. (2006). There is a range of wind property determinations in the extensive literature on ζ Pup. The terminal velocity of the wind may be as low as 2200 km s^{-1} (Lamers & Leitherer 1993), and as high as 2485 km s^{-1} (Prinja, Barlow & Howarth 1990), though we adopt the determination by the Munich group (Puls et al. 2006), of 2250 km s^{-1}, as our standard.

Mass-loss rate determinations vary as well. This is partly because of the uncertainty in the distance to ζ Pup. But, it is also the case that each mass-loss rate diagnostic is subject to uncertainty: density-squared diagnostics like Hα and free–free emission are affected by clumping, no matter the size scale or optical depth of the clumps. Mass-loss rates from UV absorption lines are subject to uncertain ionization corrections. In the last few years there have been attempts to account for clumping when deriving mass-loss rates from both density-squared diagnostics and UV absorption diagnostics. We list two recent Hα mass-loss rate determinations in the table, one that assumes a smooth wind and one that parametrizes small-scale clumping using a filling factor approach. The X-ray line profile diagnostics of mass-loss rate that we employ in this paper are not directly affected by clumping; although very large-scale porosity (associated with optically thick clumps) can affect the profiles, as we have already discussed.

The star shows periodic variability in various UV wind lines (Howarth, Prinja & Massa 1995) as well as Hα (Berghoefer et al.

Table 1. Stellar and wind parameters adopted from Puls et al. (2006).

Parameter	Value
Distance	460 pc
Mass[a]	$53.9\,\mathrm{M_\odot}$
T_{eff}	39 000 K
R_*	$18.6\,\mathrm{R_\odot}$
$v_{\mathrm{rot}}\sin i$[b]	$230\,\mathrm{km\,s^{-1}}$
v_∞	$2250\,\mathrm{km\,s^{-1}}$
β	0.9
$\dot{M}$[c]	$8.3\times10^{-6}\,\mathrm{M_\odot\,yr^{-1}}$
$\dot{M}$[d]	$4.2\times10^{-6}\,\mathrm{M_\odot\,yr^{-1}}$

[a]From Repolust, Puls & Herrero (2004).
[b]From Glebocki, Gnacinski & Stawikowski (2000).
[c]Unclumped value from Puls et al. (2006).
[d]Also from Puls et al. (2006), but the minimum clumping model, in which the far wind, where the radio emission arises, is unclumped, but the inner wind, where the Hα is produced is clumped. Note that the methodology of Puls et al. (2006) only enables a determination to be made of the *relative* clumping in different regions of the wind. This value of the mass-loss rate, therefore, represents an upper limit.

Figure 2. A visualization of the wind Doppler shift and optical depth – two effects that govern the observed, broadened and asymmetric line shapes. The observer is on the left-hand side, and the light contours represent the line-of-sight velocity in increments of $0.2v_\infty$, with the blueshifts arising in the left-hand hemisphere and the redshifts in the right-hand one. The star is the grey circle at the centre, and the inner radius of the wind X-ray emission, R_o, is indicated at $1.5R_*$ by the solid black circle. The solid heavy contour represents the locus of points with optical depth $\tau = 0.33$, and the dashed and dotted contours represent $\tau = 1$ and 3, respectively. The model parameters visualized here are nearly identical to those of the best-fitting model for the Ne x Lyα line shown in Fig. 8: $R_\mathrm{o} = 1.5$; $\tau_* = 2$.

1996). Its broad-band X-ray properties are normal for an O star, with $L_\mathrm{x} \approx 10^{-7}\,L_{\mathrm{Bol}}$ and a soft spectrum (Hillier et al. 1993), dominated by optically thin thermal line and free–free emission from plasma with a temperature of a few million degrees. The emission measure filling factor of the wind is small, roughly one part in 10^3. Weak soft X-ray variability, with an amplitude of 6 per cent, and a period of 16.7 h, was detected with *ROSAT* (Berghoefer et al. 1996). This low-level variability appears not to affect the *Chandra* data.

4 EMISSION-LINE PROFILE MODEL FITTING

4.1 The model

The X-ray emission-line profile model we fit to each line was first described by Owocki & Cohen (2001), building on work by MacFarlane et al. (1991) and Ignace (2001). It is a simple, spherically symmetric model that assumes the local emission scales as the ambient density squared and that the many sites of hot, X-ray-emitting plasma are smoothly distributed throughout the wind above some onset radius, R_o, which is expected to be several tenths of a stellar radius above the photosphere in the line-driven instability scenario (Owocki, Castor & Rybicki 1988; Feldmeier, Puls & Pauldrach 1997; Runacres & Owocki 2002). Attenuation of the emitted X-rays occurs in the bulk, cool ($T \approx T_{\mathrm{eff}}$) wind component via photoelectric absorption, mainly out of the inner shell of elements N through Si and also out of the L shell ($n = 2$) of Fe. Singly ionized helium can also make a contribution at long wavelengths. We assume that the atomic opacity of the cool wind, while a function of wavelength, does not vary significantly with radius. This is confirmed by our non-local thermal equilibrium (non-LTE) wind ionization modelling, discussed in Section 5.1. We further assume a beta-velocity law, $v = v_\infty(1 - R_*/r)^\beta$, for both wind components, with $v_\infty = 2250\,\mathrm{km\,s^{-1}}$ as given by UV observations (Puls et al. 2006). The local velocity controls the wavelength dependence of the emissivity, the local optical depth governs the wavelength-
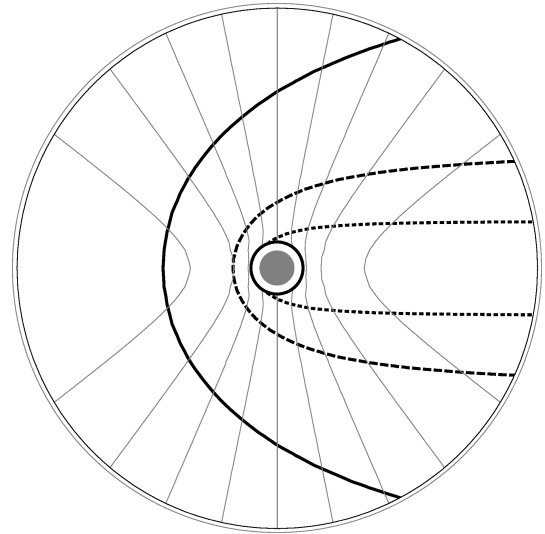
dependent attenuation, and the density affects the overall level of emission. The first two of these effects can be visualized in Fig. 2.

We cast the expression for the line profile first in spherical coordinates, but evaluate some of the quantities explicitly in terms of ray coordinates, with the origin at the centre of the star and the observer at $z = \infty$. We integrate the specific intensity along rays of given impact parameter, p, and then integrate over rays. Integrating over the volume of the wind, we have

$$L_\lambda = 8\pi^2 \int_{-1}^{+1} \mathrm{d}\mu \int_{R_\mathrm{o}}^{\infty} \eta(\mu, r) r^2 e^{-\tau(\mu, r)} \mathrm{d}r, \qquad (1)$$

where L_λ is the luminosity per unit wavelength – it is the X-ray line profile. The angular coordinate $\mu \equiv \cos\theta$, and η is the wavelength-dependent emissivity that accounts for the Doppler shift of the emitting parcel of wind material [which is completely determined, under the assumptions of spherical symmetry and the velocity law, according to its location, (μ, r) or (p, z)]. The emissivity has an additional radial dependence due to the fact that it is proportional to the square of the ambient plasma density. The optical depth, τ, is computed along a ray, $z = \mu r$, for each value of the impact parameter, $p = \sqrt{1 - \mu^2}\,r$, as

$$\tau(\mu, r) = t(p, z) = \int_z^\infty \kappa\rho(r') \mathrm{d}z', \qquad (2)$$

where the dummy radial coordinate is given by $r' \equiv \sqrt{z'^2 + p'^2}$. The opacity, κ, does not vary significantly across a line (recall it is due to continuum processes – the strong wavelength dependence across a line profile arises purely from the geometry indicated in Fig. 2). Using the continuity equation and the beta-velocity law of the wind, we have

$$t(p, z) = \tau_* \int_z^\infty \frac{R_* \mathrm{d}z'}{r'^2 (1 - R_*/r')^\beta}. \qquad (3)$$

We account for occultation of the back of the wind by the star by setting this optical depth integral to ∞ when $p < R_*$ and $z < \sqrt{R_*^2 - p^2}$. The constant at the front of equation (3), $\tau_* \equiv \kappa\dot{M}/4\pi R_* v_\infty$, is the fiducial optical depth and is equivalent to the optical depth value along the central ray, integrated down to the stellar surface, in the case where $v = v_\infty$. This quantity, τ_*, is the key parameter that describes the X-ray attenuation and governs the shifted and asymmetric form of the line profiles.

We note that the optical depth integral, while generally requiring numerical integration, can be done analytically for integer values of β. We use $\beta = 1$ throughout this paper (though we report on tests we did for non-integer β values in Section 4.3), and for that value of the parameter, the optical depth integral along a ray with impact parameter, p, is given by

$$t(p > R_*, z) = \frac{R_* \tau_*}{z_t}\left(\arctan\frac{R_*}{z_t} + \frac{\pi}{2}\right.$$
$$\left. - \arctan\frac{R_* \mu}{z_t} - \arctan\frac{z}{z_t}\right), \qquad (4)$$

$$t(p < R_*, z) = \frac{R_* \tau_*}{2z_*}\log\left(\frac{R_* - z_*}{R_* + z_*}\frac{R_* \mu + z_*}{R_* \mu - z_*}\frac{z + z_*}{z - z_*}\right), \qquad (5)$$

where $z_t \equiv \sqrt{p^2 - R_*^2}$ and $z_* \equiv \sqrt{R_*^2 - p^2}$, and the integral has been evaluated at z and ∞.

The intrinsic line profile function we assume for the emissivity at each location is a delta function that picks out the Doppler shift line resonance,

$$\eta \propto \delta\{\lambda - \lambda_o[1 - \mu v(r)/c]\}. \qquad (6)$$

This assumption is justified because the intrinsic linewidth is dominated by thermal broadening, which is very small compared to the Doppler shift caused by the highly supersonic wind flow.

Calculating a line profile model, then, amounts to solving equations (1) and (3) for a given set of parameters: R_o, τ_*, the normalization (which determines the overall level of η), and an assumed wind velocity law, described by β and v_∞. This last parameter, v_∞, influences the emissivity term through its effect on the Doppler shift as a function of radius and spherical polar angle. And for our choice of $\beta = 1$, equations (4) and (5) replace equation (3).

The model produces broad emission lines where the overall width (in the sense of the second moment of the profile), for an assumed wind velocity law, is governed primarily by the parameter R_o. The closer to the star's surface R_o is, the more emission there is from low-velocity wind material, which contributes to the line profile only near line centre. The value of τ_* affects the line's blueshift and asymmetry. The higher its value, the more blueshifted and asymmetric the profile. Large values of τ_* also reduce the profile width by dramatically attenuating the redshifted emission component of the line. The interplay of the two parameters can be seen in fig. 2 of Owocki & Cohen (2001).

4.2 Fitting the data

4.2.1 Statistical fitting of individual lines

For each line in the spectrum, our goal is to extract values for the two parameters of interest – τ_* and R_o – and to place formal confidence limits on these values. We begin the analysis procedure for each line by fitting the weak continuum simultaneously in two regions, one to the blue side of the line and one on the red side (but excluding the wavelength range of the line itself). We assume the continuum is flat over this restricted wavelength region. We then fit the emission

line over a wavelength range that is no broader than the line itself (and sometimes even narrower, due to blends with nearby lines, which can induce us to exclude contaminated portions of the line in question). The model we fit to each line is the sum of the empirical line profile model – described by equations (1), (4) and (5) – and the continuum model determined from the fit to the two spectral regions near the line. Note that the inclusion of the continuum does not introduce any new free parameters. The overall model thus has only three free parameters: the fiducial optical depth τ_*, the minimum radius of X-ray emission R_o and the normalization of the line. In some cases, where lines are blended, we fit more than one profile model simultaneously, as we describe below, but we generally keep the two main parameters of each profile model tied together, and so the only new free parameter introduced is an additional line normalization.

We fit the wind profile plus continuum model to both the MEG and HEG data (positive and negative first orders) simultaneously, if the HEG data are of good enough quality to warrant their inclusion, and to the MEG data only if they are not. We use the C statistic (Cash 1979) as the goodness-of-fit statistic. This is the maximum likelihood statistic for data with Poisson-distributed errors, which these photon-counting X-ray spectra are. Note that the maximum likelihood statistic for Gaussian-distributed data is the well-known χ^2 statistic, but it is not valid for these data, which have many bins with only a few counts, especially in the diagnostically powerful wings of the profiles.

We determine the best-fitting model by minimization of the C statistic using the 'fit' task in XSPEC. Once the best-fitting model is found, the uncertainties on each model parameter are assessed using the $\Delta\chi^2$ formalism[1] outlined in chapter 15 of Press et al. (2007), which is also valid for ΔC. We test each parameter one at a time, stepping through a grid of values and, at each step, refit the data while letting the other model parameters be free to vary. The 68 per cent confidence limits determined in this manner are what we report as the formal uncertainties in the table of fitting results, below. We also examine the confidence regions in two-dimensional subspaces of the whole parameter space in order to look for correlations among the interesting parameters. Note that we include an extensive discussion of modelling uncertainties in Section 4.3.

We use the relatively strong and unblended Fe XVII line at 15.014 Å to demonstrate this fitting process. We show the MEG and HEG data for this line, along with the best-fitting model (the set of model parameters, τ_*, R_o, and normalization that minimizes the C statistic) in Fig. 3. The best-fitting model parameters are: $\tau_* = 1.97$, $R_o = 1.53 R_*$, and a normalization of 5.24×10^{-4} photons s^{-1} cm^{-2}. Using the ΔC criterion and testing each of these parameters one at a time (while allowing each of the other parameters to vary), we find that the 68 per cent confidence limits on the fit parameters are $1.63 < \tau_* < 2.35$, $1.38 < R_o/R_* < 1.65$ and $5.04 \times 10^{-4} <$ norm $< 5.51 \times 10^{-4}$. The confidence limits should be thought of as probabilistic statements about the chance that the true parameter values lies within the given range, given the physical assumptions of the model.

In Fig. 4 we show 68, 90 and 95 per cent confidence limits in two-dimensional τ_*, R_o parameter space. We calculate a grid of models (typically 36×36), optimizing the other free parameters (just the normalization, in this case) at each point in the grid, and use values of $\Delta C = 2.30$, 4.61 and 6.17 (Press et al. 2007) to define the

---

[1] This criterion is a specific numerical value of $\Delta C \equiv C_i - C_{\min}$ for model realization i, where $C_{\min}$ is the C statistic value for the best-fitting model.
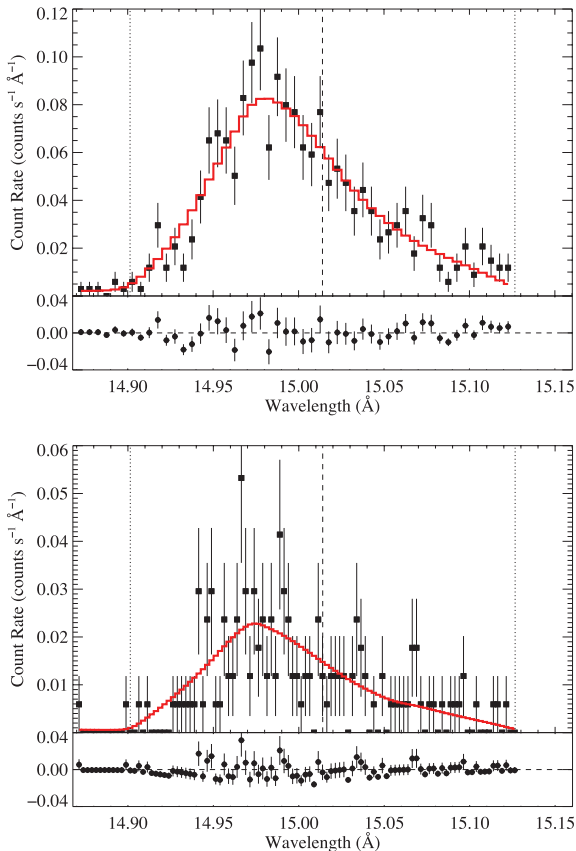
Figure 3. The Fe XVII line at 15.014 Å in the MEG (top) and HEG (bottom), with the best-fitting model superimposed. We have not done any rebinning of the data. The error bars represent Poisson, root-N statistics. The dashed vertical lines indicate the laboratory rest wavelength of the emission line, and the two dotted vertical lines in each panel indicate the wavelengths associated with the Doppler shift due to the stellar wind terminal velocity of 2250 km s^{-1}. The model is shown as the thick (red in on-line version) histogram, while the data are shown as (black) solid squares with error bars. The fit residuals are shown in the horizontal windows below the data, with the same 1σ error bars that are shown with the data.
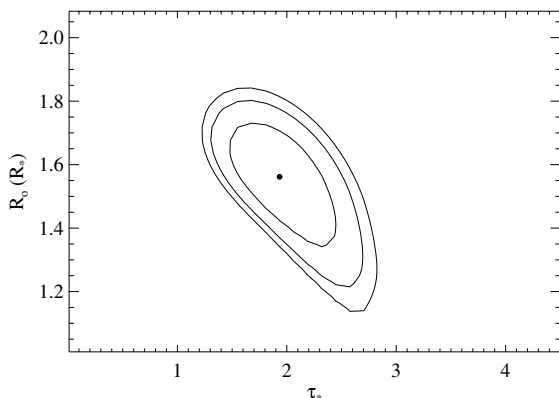

Figure 4. Confidence contours (68, 90 and 95 per cent) for the model fitting of the Fe XVII line at 15.014 Å. The best fit, shown in Fig. 3, is represented by the filled circle.

extent of the confidence limits. Plots such as this one are a good means of examining correlations between model parameters, in terms of their abilities to produce similar features in the line profiles. We can see what the trade offs are between parameters in a

quantitative way. For example, there is a modest anticorrelation between R_o and τ_* evident in the figure. Low values of R_o (shock onset close to the photosphere) reduce emission on the line wing relative to the core (because there is more emitting material at low velocity). So although low values of R_o (hot plasma as close as 1.15R_*) are allowed at the 95 per cent confidence limit, they require a large wind optical depth, $\tau_* \approx 3$, to compensate. High τ_* values make lines narrower, as small values of R_o do, but they also cause lines to be more blueshifted and asymmetric. So, there is some degeneracy between these two parameters, but it can be broken for good-quality data. We note that the confidence limits listed in the table of model fitting results, which are for individual parameters considered one at a time, will tend to differ somewhat from those inferred from these plots of joint confidence limits.

The value of τ_* at $\lambda = 15$ Å expected from the smooth-wind Hα mass-loss rate (Puls et al. 2006) is $\tau_* = 5.30$, using the opacity model described in Section 5.1 (which gives a value of $\kappa = 37$ cm^2 g^{-1} at 15 Å). The best-fitting model with fixed $\tau_* = 5.30$ is shown in Fig. 5. This model does not provide a good fit, having $\Delta C = 64$, implying rejection probabilities well above 99.99 per cent. This is the quantitative basis for claims that the X-ray emission lines of O stars in general, and ζ Pup in particular, are too symmetric and unshifted to be explained by the standard wind-shock scenario (Cassinelli et al. 2001; Kahn et al. 2001; Kramer et al. 2003; Oskinova et al. 2006). However, the primary goal of this paper is to quantify the mass-loss rate by modelling the wind opacity and the effects of wind attenuation on all the line
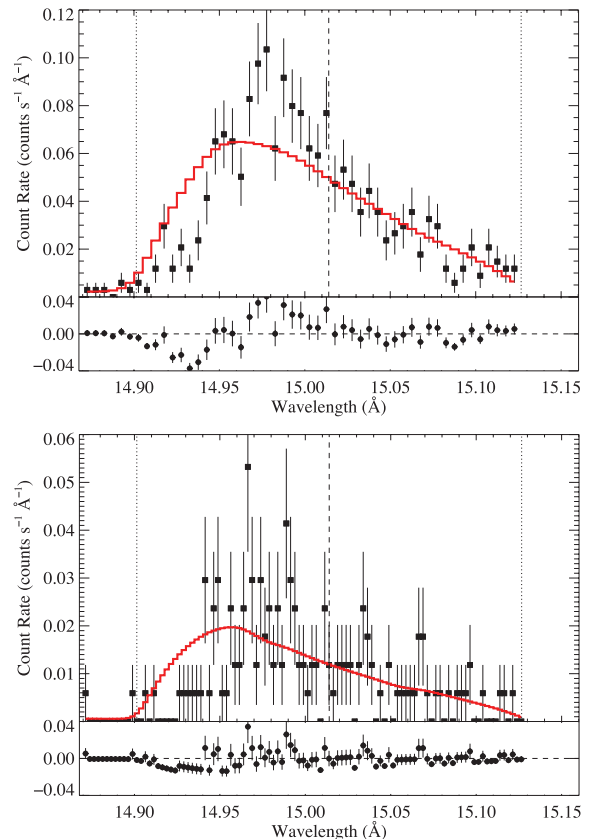

Figure 5. The Fe XVII line at 15.014 Å in the MEG (top) and HEG (bottom), with the best-fitting model having $\tau_* = 5.30$ superimposed. This is the value implied by the smooth-wind Hα mass-loss rate and our wind opacity model. The normalization and R_o were the adjustable parameters of this fit. Even this best-fitting model is statistically unacceptable.

profiles together. To enable us to do this, we repeat the fitting procedure described above for all 21 of the lines and line complexes in the spectrum that have more than 50 counts.

4.2.2 Fitting helium-like line complexes

For the helium-like complexes – O VII, Ne IX, Mg XI, Si XIII and S XV – we fit a modified version of the wind profile model in XSPEC that simultaneously fits three separate profiles with the basic parameters (τ_* and R_o) tied together. It accounts for the altered forbidden-to-intercombination line strength ratios due to the effects of photoexcitation out of the 2^3S state, which is the upper level of the forbidden line. This model, which was first described in Leutenegger et al. (2006), assumes a spatial distribution of X-ray-emitting plasma, just as the basic wind profile model does, but alters the radius-dependent line ratio according to the UV mean intensity computed from an assumed model atmosphere.[2] This model thus self-consistently accounts for the effects of the radial dependence of the individual line emissivities on both the line ratio and the profile shapes. Although the components of these complexes are blended, we can extract useful model parameters and confidence limits on those parameters by fitting each complex as a single entity.

4.2.3 Line blends

We handle other line blends in a manner similar to the helium-like complexes, simultaneously fitting profile models with parameters tied together. However, some blends – composed of lines from different ionization states or different elements – are more problematic, as their relative strengths are generally more uncertain. In some cases, the blending is mild – through a combination of the second line being weak and the overlap region being small – and we can fit the stronger of the components reliably by simply excluding some of the data. This was the case for the Ne X Lyα line at 12.134 Å, where the extreme red wing is mildly blended with a weak iron line. In other cases, like the Fe XVII lines at 17.051 and 17.096 Å, where the relative intensities of the components are well constrained by atomic physics, we obtain reliable results. But this situation is generally only true when the overlap between lines is modest and, especially, when both lines arise from the same ionization state of the same element, as is the case for these Fe XVII lines.

There are, however, several blends where the modelling of the relative line strengths is simply too uncertain to draw any reliable conclusions. A good example of this is the N VII Lyα line at 24.781 Å, which is blended with the N VI Heβ line at 24.890 Å. For this line blend we fit a series of models with two components – one for the Lyα line and one for the Heβ line – trying different values of their relative normalizations, all within a plausible range (of 0.1–0.4) as implied by the Astrophysical Plasma Emission Database (APED) (Smith et al. 2001). We found values for the fiducial optical depth, τ_*, ranging from less than 1 to more than 4. These constraints are nearly meaningless, and thus we exclude the results for this blended line complex from the overall analysis described in Section 5.

The five line blends that could not be reliably fit are indicated in Fig. 1 by the dashed vertical lines between the panels. We stress that we fit all five of these complexes with multiple profile models,

and in each case found that it was impossible to put reliable constraints on τ_* and R_o, given the wide range of possible relative line normalizations. In addition to the N VII and N VI blend near 24.8 Å, the complexes that we had to reject include the helium-like neon complex near 13.5 Å, which is blended with at least seven iron lines that have relative strengths which are temperature dependent, and the O Lyβ line at 16.006 Å, which is blended with four Fe XVIII lines, and two complexes near 11.0 and 15.26 Å that contain numerous weak lines arising from Fe XVI, Fe XVII and several higher ionization states of iron.

4.2.4 Results

After eliminating the five line complexes too blended to give meaningful results, we are left with 16 lines and line complexes that could be fitted with the wind profile model as described in the previous subsection and as demonstrated on the Fe XVII line at 15.014 Å. The results of these fits are summarized in Table 2. And we show four more representative line fits – spanning a wide range of wavelengths and derived values of τ_* – in Figs 6–9. Note the progression in these profiles from fiducial optical depths, τ_*, close to zero at the shortest wavelengths to significantly larger values (up to $\tau_* = 3$) at the longest wavelengths. We summarize the 16 derived τ_* and R_o values, along with their confidence limits, in Fig. 10.

4.3 Sensitivity of fitting results to modelling assumptions

We have made various assumptions and choices in carrying out the line profile modelling described in the previous subsection. And we therefore have investigated many of these, again using the Fe XVII line at 15.014 Å as a test case. In this subsection, we report on the sensitivity of our results to the following assumptions and choices: background subtraction; determination of the continuum level; exclusion of portions of the line due to possible blending; inclusion of the weak HEG data; the adopted values of β and v_∞ for the wind and whether to allow the X-ray volume filling factor to vary with radius [as parametrized by q in $f_X \propto r^{-q}$, where the filling factor, f_X, contributes to the emissivity, η – see Owocki & Cohen (2001)]. We will very briefly describe those factors that we found to be unimportant, and discuss in more detail those that did make a difference. The baseline model fitting we describe here is the modelling described in the previous subsection for the 15.014 Å line, except that we fit only the MEG data (so that we may evaluate the effect of including the HEG data).

We examined the default background spectra, which were very weak, and also experimented with fitting the 15.014 Å line with and without the background spectrum subtracted and found almost no difference in the fit quality or fit parameters. We therefore opt to neglect the background when fitting each of the lines in the spectrum. The sensitivity to the continuum fit is a little greater, but still nearly negligible. When we changed the continuum level by a factor of 2 – which is larger than the formal uncertainty on the continuum level – none of the parameter values changed by more than 10 per cent. Some lines in the spectrum are blended with weaker lines. The cleanest way to handle this situation is to exclude the contaminated bins from the modelling. To test the effects of this, we eliminated 0.03 Å from the red wing of the 15.014 Å line and refit the data. We then repeated this experiment eliminating 0.07 Å – leaving only about two-thirds of the data. Even in this second, extreme case, the fit parameters varied by less than 10 per cent and the confidence regions only expanded slightly.

For most lines, the HEG data are significantly weaker than the MEG data. We find for the 15.014 Å line that including the HEG

---

[2] TLUSTY O star model (Lanz & Hubeny 2003) with $T_{eff} = 40\,000$ K and $\log g$ interpolated between 3.50 and 3.75.

Table 2. Wind profile model fit results.

Ion	Wavelength[a] (Å)	τ_*	$R_{\rm o}$ (R_*)	Normalization[b] (10^{-5} photons cm^{-2} s^{-1})
S xv	5.0387, 5.0648, 5.1015	$0.01^{+0.36}_{-0.01}$	$1.41^{+0.15}_{-0.11}$	$2.56^{+0.24}_{-0.36}$
Si xiv	6.1822	$0.49^{+0.61}_{-0.35}$	$1.46^{+0.20}_{-0.14}$	$0.77^{+0.11}_{-0.14}$
Si xiii	6.6479, 6.6866, 6.7403	$0.42^{+0.14}_{-0.13}$	$1.50^{+0.06}_{-0.04}$	$11.2^{+0.4}_{-0.4}$
Mg xi	7.8503	$0.65^{+0.19}_{-0.32}$	$1.33^{+0.12}_{-0.13}$	$1.33^{+0.17}_{-0.13}$
Mg xii	8.4210	$1.22^{+0.53}_{-0.45}$	$1.34^{+0.18}_{-0.21}$	$2.95^{+0.24}_{-0.24}$
Mg xi	9.1687, 9.2297, 9.3143	$0.92^{+0.19}_{-0.16}$	$1.55^{+0.06}_{-0.06}$	$17.8^{+0.8}_{-0.5}$
Ne x	9.7082	$0.62^{+1.05}_{-0.52}$	$1.48^{+0.27}_{-0.19}$	$0.95^{+0.15}_{-0.15}$
Ne x	10.2388	$1.95^{+0.28}_{-0.87}$	$1.01^{+0.45}_{-0.00}$	$2.99^{+0.31}_{-0.29}$
Ne ix	11.5440	$0.83^{+0.65}_{-0.44}$	$2.08^{+0.54}_{-0.36}$	$5.00^{+0.40}_{-0.50}$
Ne x	12.1339	$2.03^{+0.24}_{-0.28}$	$1.47^{+0.11}_{-0.10}$	$26.9^{+1.1}_{-0.7}$
Fe xvii	15.014	$1.94^{+0.32}_{-0.33}$	$1.55^{+0.13}_{-0.12}$	$52.4^{+2.5}_{-1.6}$
Fe xvii	16.780	$2.86^{+0.38}_{-0.71}$	$1.01^{+0.61}_{-0.00}$	$23.1^{+1.9}_{-1.2}$
Fe xvii[c]	17.051, 17.096	$2.52^{+0.70}_{-0.64}$	$1.47^{+0.35}_{-0.46}$	$32.7^{+0.9}_{-1.1}$
O viii	18.969	$3.02^{+0.52}_{-0.57}$	$1.18^{+0.41}_{-0.17}$	$37.0^{+2.8}_{-2.6}$
N vii	20.9099	$4.26^{+2.28}_{-1.71}$	$1.88^{+0.87}_{-0.87}$	$14.8^{+2.3}_{-1.9}$
O vii	21.602, 21.804	$1.62^{+1.33}_{-0.79}$	$2.53^{+0.85}_{-0.50}$	$59.9^{+4.9}_{-5.4}$

[a]Closely spaced doublets in the Lyman series lines and He-like intercombination lines are fitted with a single profile model centred at the emissivity-weighted wavelength of the two components.
[b]For the blended lines fitted simultaneously, including the He-like complexes, the total normalization of all the lines in the complex is indicated.
[c]We fit these two blended lines simultaneously, with a fixed normalization ratio of 0.9. Both line profile components were forced to have the same τ_* and $R_{\rm o}$ values. Allowing the intensity ratio to vary between 0.8 and 1.0 hardly changed the parameter confidence limits at all.

data changes the best-fitting model parameters by, at most, a few per cent, but it does tighten the confidence limits somewhat. The effect of including the HEG data is more significant for the shorter wavelength lines, where the effective area of the HEG is larger relative to the MEG. There is very little penalty for including the HEG data, so we do so for all lines shortward of 16 Å. We also fit the MEG and HEG data separately for the 15.014 line to verify that there are not systematic effects between these two spectra; and there are not. The separate fits give results that are very similar to each other, with significantly overlapping 68 per cent confidence limits for all parameters.

The original Owocki & Cohen (2001) line profile model allows for a radially varying filling factor of X-ray-emitting plasma, parametrized as a power-law function of radius. Values of the power-law index q that differ significantly from zero (no radial variation) can cause changes in the line profiles that are not insignificant, effectively weighting the emission from parts of the wind according to their velocity (via the beta-velocity law relationship between velocity and radius). However, we find that when we allow q to be a free parameter the best-fitting value is generally very close to zero. For the representative 15.014 Å line, it is $q = -0.09$, and $q = 0$ is included in the 68 per cent confidence range. The general result is consistent with that found for this and other stars (Kramer et al. 2003; Cohen et al. 2006). Thus, to keep the number of free parameters manageable, we fix $q = 0$.

The factors discussed above have a very minor influence on the results of the line fitting. However, the remaining factors can have a significant effect.

The velocity-law exponent, β, affects line profiles for two reasons: (1) the velocity law affects the mapping between radius and Doppler-shifted wavelength, and so affects the emission profile and

(2) via the continuity equation, it affects the density and so affects the level of both the emission and the absorption. Indeed, for our representative emission line, when we change the value of β from 1 to 0.8, both τ_* and $R_{\rm o}$ change by 10–20 per cent. The determinations of β for ζ Pup vary from at least 0.9 to 1.15, and so using a value of $\beta = 1$ seems reasonable, especially as it speeds the calculation of the line profile model by allowing the optical depth integral to be done analytically, so we use that value for all the model fitting results reported here. If, in the future, a new and more accurate determination of β is made, and it differs significantly from $\beta = 1$, then the results reported in this paper can be scaled accordingly.[3] We also note that the X-ray-emitting plasma and the bulk wind that attenuates the X-rays may not necessarily be described by the same beta velocity law. However, there is no independent evidence for this, and with the short post-shock cooling lengths expected in the relatively dense wind of ζ Pup, the X-ray-emitting plasma in the wind is more likely to have a velocity close to the ambient wind velocity.[4] And furthermore, the observed X-ray emission linewidths in ζ Pup and other early O supergiants are completely consistent with the β and v_∞ values inferred from UV and optical spectroscopy of these stars.

---

[3] Lowering β from 1 to 0.8 causes the best-fitting optical depth of the Fe xvii line at 15.014 Å to go from $\tau_* = 1.98$ to 1.66. If the value of β were to be revised upward by a similar amount, the values we derive for τ_* from the line profile fitting would have to be revised upward by about 15 per cent. The quality of the fits with the different values of β do not differ significantly.
[4] X-ray-emitting plasma is too highly ionized to be effectively driven by the photospheric UV radiation field. However, for small enough parcels, the ram pressure of the surrounding wind should keep the post-shock, hot plasma moving at the ambient velocity.
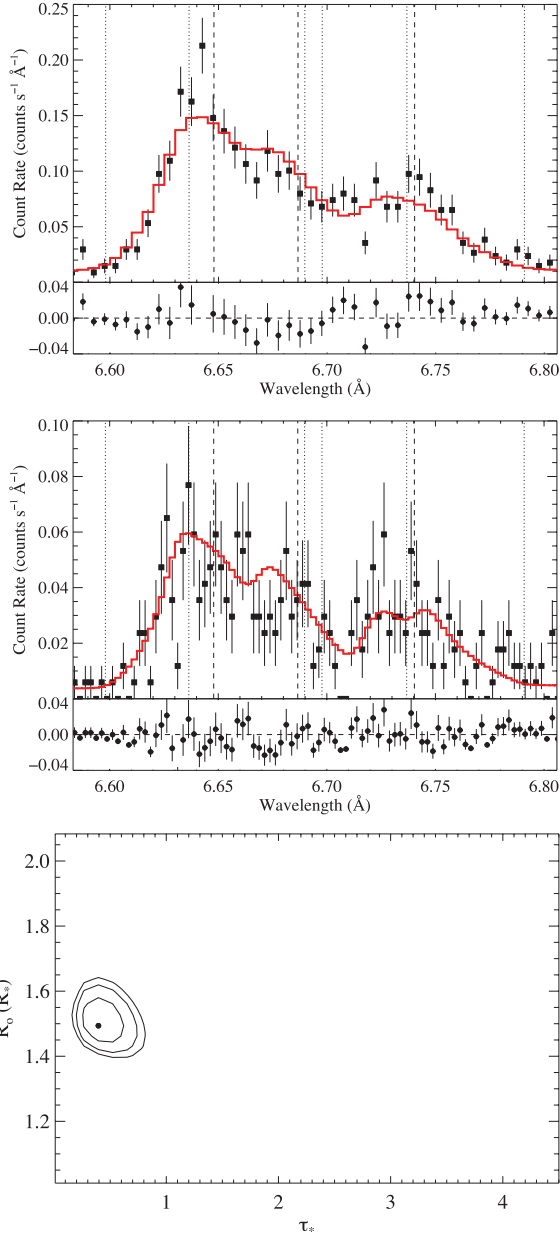
Figure 6. The MEG (top) and HEG (middle) measurements of the Si XIII helium-like complex near 6.7 Å, along with the best-fitting model. This line complex shows a relatively small degree of blueshift and asymmetry, indicative of a low τ_* value, as is expected at short wavelengths, where the wind opacity is smaller. Note that there is a separate set of vertical lines – denoting the rest wavelength and the Doppler shifts associated with the wind terminal velocity – for each of the three components of the line complex (resonance, intercombination and forbidden lines, from short to long wavelength). In this and the following three figures, we also show the 68, 90 and 95 per cent confidence limits in τ_*, R_o parameter space (bottom).

The terminal velocity of ζ Pup is relatively well established, with reasonable estimates from several different groups that vary by about ± 10 per cent about our adopted value of $2250\,\mathrm{km\,s^{-1}}$. However, when we explored the effect of varying the terminal velocity in our fitting of wind profile models to the 15.014 Å line, we found that the value of τ_* was quite sensitive to the assumed wind terminal velocity, even within this relatively narrow range. This
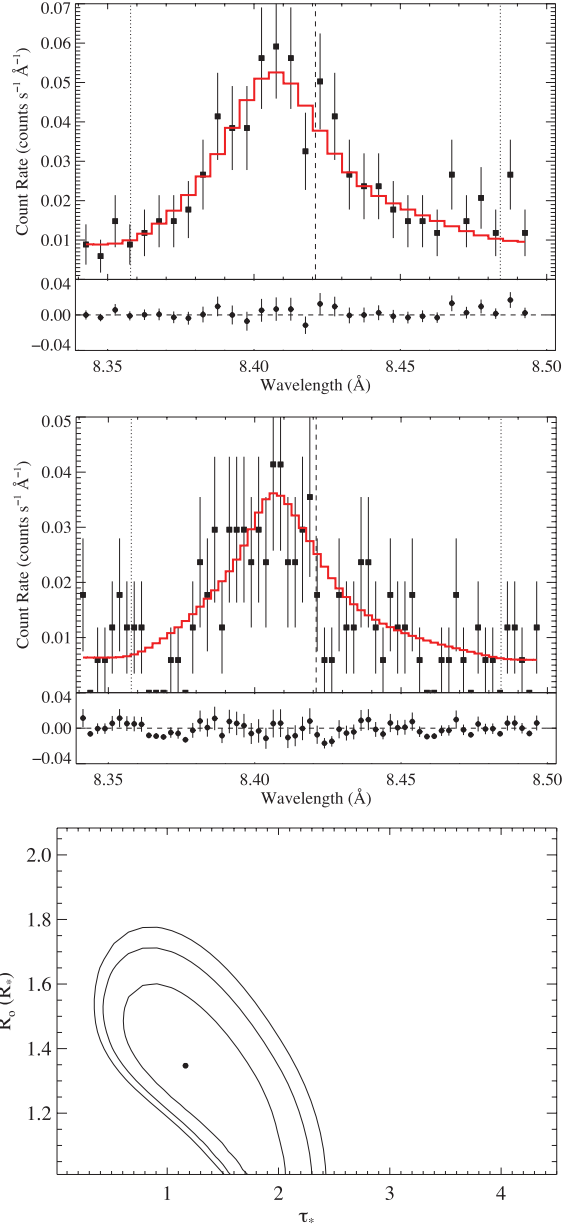
Figure 7. The derived value of τ_* is also low for the Mg XII Lyα line at 8.421 Å shown here, but it is modestly higher than the shorter wavelength Si XIII complex shown in the previous figure.

is because the blueshift of the line centroid in the dimensionless, scaled wavelength parameter, $x \equiv (\lambda/\lambda_o - 1)c/v_\infty$, depends directly on the degree of wind absorption. The same observed profile appears more blueshifted in scaled wavelength units if the terminal velocity is (assumed to be) smaller. Our tests with the 15.014 Å line show that the best-fitting value for τ_* ranges from 2.16 to 1.35 when we use terminal velocities between 2200 and 2485 km s^{-1}. This variation is larger than that caused by every other parameter uncertainty and assumption we have explored. Thus, while we consider the value of $v_\infty = 2250\,\mathrm{km\,s^{-1}}$ to be quite reliable, future re-assessments of this parameter will necessitate a rescaling of the optical depth – and mass-loss rate – results we report in this paper.

As a final test, we can treat the terminal velocity as a free parameter of the model. This enables us to see what value of the terminal
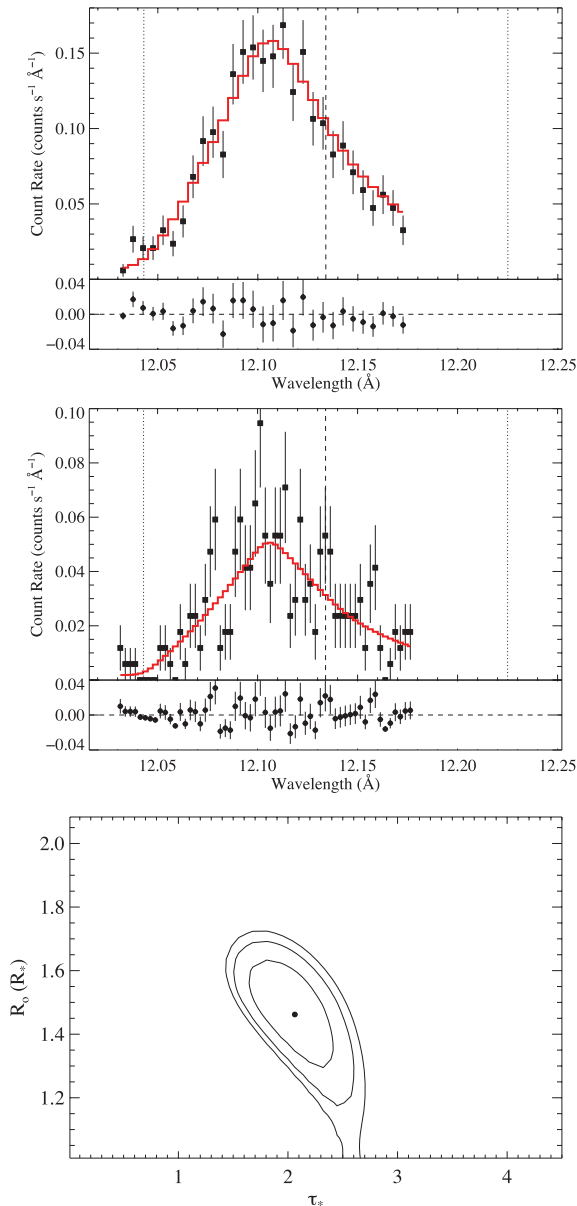
Figure 8. The Ne X Lyα line at 12.134 Å shows an intermediate degree of blueshift and asymmetry, indicative of an intermediate τ_* value, as is expected at its wavelength, where the wind opacity is larger than at the wavelength of the Mg XII Lyα line, but not as large as at longer wavelengths. Part of the red wing of this line has been excluded from the fitting because of a possible blend with an iron line.

velocity is preferred by the X-ray spectral data themselves. In general, the constraints on v_∞, while letting the other model parameters be free to vary, were not strong. But for the highest signal-to-noise ratio lines in the spectrum, relatively tight constraints could be derived. We show the results for fitting the five most useful lines in Fig. 11. As the figure shows, these lines are all consistent with our adopted value of $v_\infty = 2250\,\mathrm{km\,s^{-1}}$. This, of course, gives us added confidence that the value we use for the model fitting is reasonable. And, in fact, the small error bars on most of these determinations also show that significantly smaller and larger values are ruled out. The kinematics of the hot, X-ray-emitting plasma seem to be the same as that of the bulk wind for ζ Pup.
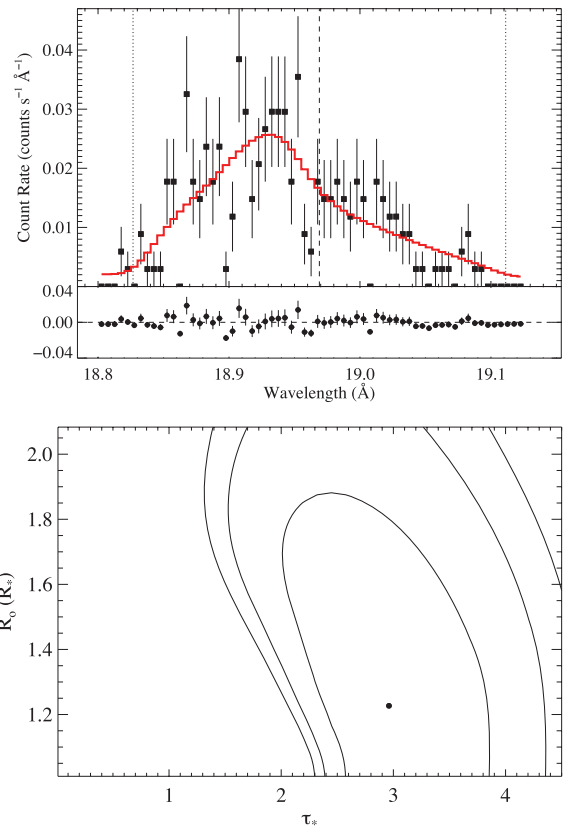

Figure 9. The O VIII Lyα line at 18.969 Å shows a relatively large degree of blueshift and asymmetry, indicative of a higher τ_* value, as is expected at longer wavelengths, where the wind opacity is larger. We did not include the very weak HEG data in the analysis of this line.

5 DISCUSSION

The most obvious new and significant result of the profile model fitting is the wavelength trend in the derived values of the fiducial optical depth, τ_*, shown in the top panel of Fig. 10. The value of this parameter, which is proportional to both the mass-loss rate and the opacity of the bulk wind, increases with wavelength, which is exactly what is expected from the form of the atomic opacity. The null hypothesis of a constant value of τ_* is rejected with greater than 99.9 per cent confidence ($\chi^2_\nu = 5.4$ for 15 degrees of freedom). We therefore fit a model of wavelength-dependent τ_*, in which the wavelength dependence derives entirely from the atomic opacity, $\kappa(\lambda)$.

While it may seem obvious that there should be a trend in the fiducial optical depth with wavelength, this result is quite significant, in that a presumed lack of such a trend is the basis for claims that large-scale clumping and the associated wind porosity are the cause of the smaller than expected profile blueshifts and asymmetry (Oskinova et al. 2006). In the following subsections, we show how a realistic wind opacity model naturally explains the observed wavelength trend, and then how such a model can be used to make a quantitative determination of the mass-loss rate of ζ Pup.

5.1 The opacity model and the mass-loss rate determination

The opacity model depends on the abundances and, to a lesser extent, the ionization balance of the bulk stellar wind (i.e. the cooler, unshocked component). The dominant source of opacity is
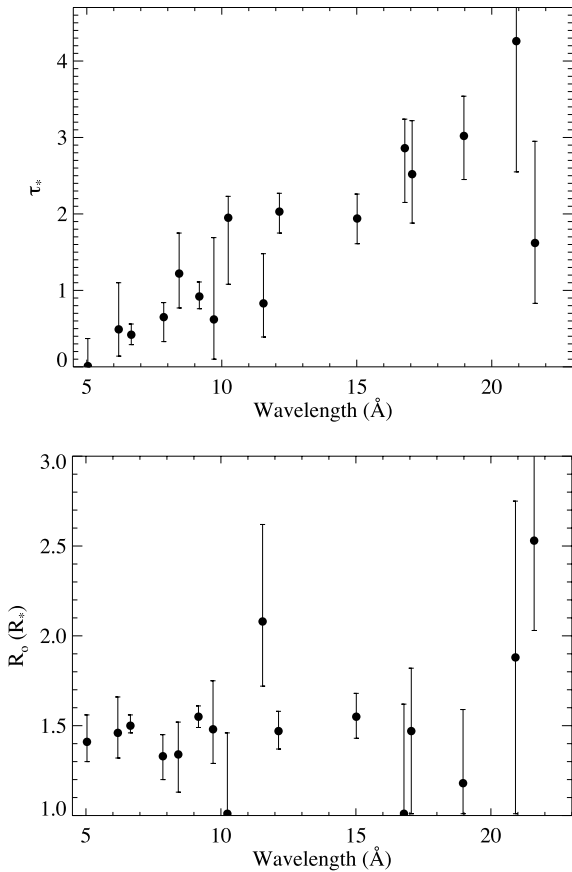
Figure 10. Values of τ_* (top) and R_o (bottom) derived from the model fits, shown with their 68 per cent confidence limits. Line complexes and blends that were fitted with multiple model components are represented by only one point.
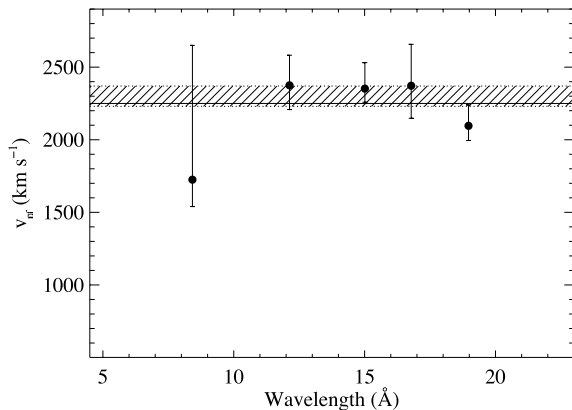

Figure 11. Values of the terminal velocity derived from fitting five strong lines with a wind profile model for which v_∞ was allowed to be a free parameter (the other parameters – τ_*, R_o and the normalization – were allowed to vary as well). The bulk wind terminal velocity adopted from the analysis of UV profiles is indicated by the solid horizontal line. The cross-hatched area represents the 68 per cent confidence region for the value of the terminal velocity derived from fitting these five points.

photoelectric absorption from the K shell of abundant elements between N and Si, and also the L shell of Fe. We have computed a wind opacity model using CMFGEN (Hillier & Miller 1998; Zsargó et al., in preparation) to model the ionization balance and using
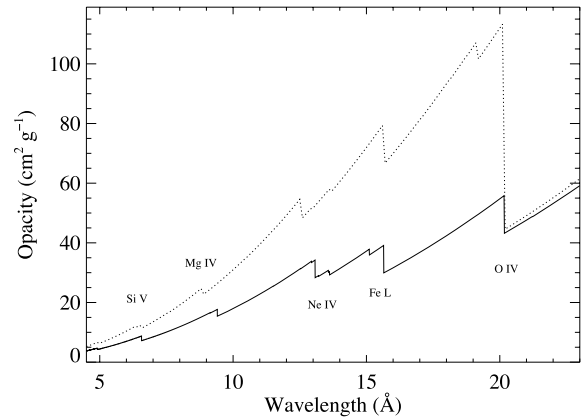

Figure 12. The wavelength dependent opacity of the wind of ζ Pup computed using CMFGEN modelling of the ionization balance and subsolar abundances derived from UV and optical spectra (solid), along with a solar abundance opacity model (dotted). Note the prominent K-shell edge of oxygen near 20 Å in the solar abundance model. In the subsolar metallicity opacity model, this decrement is much more modest, due to the underabundance of O and overabundance of N. The overall reduction in the opacity at most wavelengths in the CMFGEN model is the result of its overall subsolar metallicity and not its altered CNO abundances.

atomic cross-sections from Verner & Yakovlev (1995). The model is constrained by UV and optical spectra, so the abundances are derived directly from observations. Details are provided in (Bouret et al., in preparation) and in Bouret et al. (2008) where the overall modelling is briefly described and excellent fits to Hα and P v profiles are shown. Specifically, it is found that $Y_{\rm He} = 0.16$ [$(Z/Z_\odot)_{\rm He} = 1.88$ expressed as a fraction of the solar abundance], $(Z/Z_\odot)_{\rm C} = 0.08$, $(Z/Z_\odot)_N = 5.0$, $(Z/Z_\odot)_{\rm O} = 0.20$ and $(Z/Z_\odot)_{\rm Fe} = 1.0$, where the reference solar abundances are taken from Asplund, Grevesse & Sauval (2005). These abundances are consistent with those derived from independent analysis by the Munich group (J. Puls, private communication; Pauldrach 2003). Additionally, the low oxygen abundance is consistent with the value found from modelling the X-ray spectrum (0.30 ± 0.43; Zhekov & Palla 2007). These authors also find a high nitrogen abundance of 3.2 ± 0.6, only slightly lower than the value we adopt here. Note that we have scaled the abundances reported by Zhekov & Palla (2007) to the reference solar abundances of Asplund et al. (2005).

We show the wind opacity model, using our adopted abundances and the ionization balance from the CMFGEN modelling, at a single radius ($r = 1.8R_*$)[5] in Fig. 12, along with a solar abundance model. The opacity is lower at most wavelengths in the CMFGEN model primarily because the total abundance of metals (and most crucially the sum of carbon, nitrogen and oxygen) is subsolar [0.53 of the Asplund et al. (2005) value]. We refer to this opacity model, based on the CMFGEN modelling and the abundances derived from the UV and optical spectra, as the 'subsolar metallicity' model in the remainder of the paper.

---

[5] We note that there is very little variation in the opacity with radius between $1.1R_*$ and roughly $4R_*$ (at least at wavelengths where we analyse lines, below the nitrogen K-shell edge near 26 Å). By $5R_*$ the overall opacity is about 20 per cent higher, and by $11R_*$ it is about a factor of 2 higher. The increasing opacity with radius is due to the larger fraction of singly ionized helium in the outer wind. But the wind density is so low at these distances that the outer wind does not contribute significantly to the X-ray optical depth.
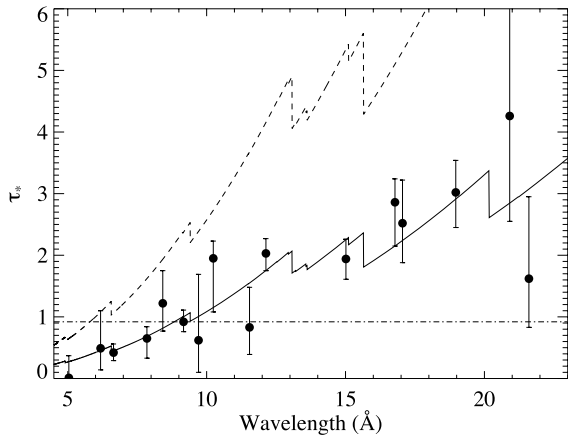
Figure 13. Values of τ_* derived from the line profile model fits, shown as points with error bars (same as the top panel of Fig. 10). The value of τ_* expected if the mass-loss rate is $8.3 \times 10^{-6}\,M_\odot\,\mathrm{yr}^{-1}$ is shown as the upper dashed curve. Treating the mass-loss rate as a free parameter, the best-fitting value of $3.50 \times 10^{-6}\,M_\odot\,\mathrm{yr}^{-1}$ is shown as the lower, varying solid curve. This model provides a formally good fit. And both of these models of the wavelength-dependent τ_* use the subsolar metallicity (CMFGEN) opacity model. The horizontal dash–dotted line is the best-fitting constant τ_* model, as would be expected for a highly porous wind, where the effective opacity is completely determined by the macroscopic, physical cross-sections of the optically thick clumps. It does not provide a good fit to the data.

Using either of these models of the opacity, and values for the stellar radius and wind terminal velocity from Table 1, we can construct a wavelength-dependent model of τ_*, for which the mass-loss rate is the only free parameter. Fits with both the subsolar metallicity wind opacity model and the solar abundance model are good ($\chi_\nu^2 \approx 0.6$ for the subsolar metallicity model and $\chi_\nu^2 \approx 0.8$ for the solar abundance model), although a higher mass-loss rate of $\dot{M} = 3.50 \times 10^{-6}\,M_\odot\,\mathrm{yr}^{-1}$ is found with the subsolar metallicity model, due to its lower overall opacity. The solar abundance opacity model, which should provide a lower limiting case, gives $\dot{M} = 1.90 \times 10^{-6}\,M_\odot\,\mathrm{yr}^{-1}$. The formal uncertainties on these derived mass-loss rates, due solely to the finite error bars on the individual τ_* determinations, are about 10 per cent.

The best-fitting τ_* model, using the subsolar metallicity opacities and the best-fitting mass-loss rate, is shown in Fig. 13, along with the τ_* model computed using the smooth-wind Hα mass-loss rate, $\dot{M} = 8.3 \times 10^{-6}\,M_\odot\,\mathrm{yr}^{-1}$. The best-fitting mass-loss rate is almost a factor of 3 lower.[6] If solar abundances are assumed for the opacities, the factor is more than 4. The best-fitting versions of these two models are compared in Fig. 14, and have a very similar shape, implying that even with better quality *Chandra* data it would be difficult to distinguish them based on the X-ray data alone. We stress, though, that the abundances of ζ Pup are certainly not solar. We

---

[6] The mass-loss rate we derive here from the X-ray line profiles is nearly identical to the Hα and radio mass-loss rate determined by Lamers & Leitherer (1993), although this is purely coincidental. Several systematic errors in Lamers & Leitherer (1993) reduce their smooth-wind mass-loss rate determination, compared to more modern estimates such as the one we employ for the fiducial, unclumped mass-loss rate (Puls et al. 2006). The factors that lead to the low value in Lamers & Leitherer (1993) include assuming that helium is fully ionized in the outer wind, ignoring departures from LTE and assuming a lower temperature than more modern analyses use, and assuming that the Hα line is optically thin.
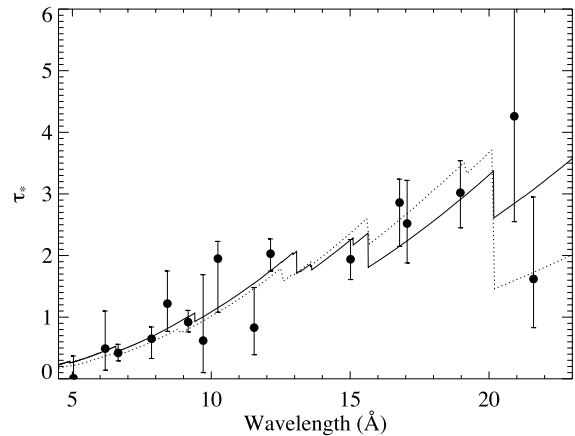

Figure 14. The best-fitting model, with $\dot{M} = 3.50 \times 10^{-6}\,M_\odot\,\mathrm{yr}^{-1}$, shown in Fig. 13, is shown here again, but this time it is compared to the best-fitting solar abundance τ_* model (dotted curve). The fits are of similar quality, while the solar abundance model has a lower mass-loss rate ($\dot{M} = 1.90 \times 10^{-6}\,M_\odot\,\mathrm{yr}^{-1}$) to compensate for its higher overall opacity.

present this model only for comparison with the subsolar metallicity opacity model, and as a limiting high-opacity case.

Taking a closer look at the atomic opacity, we can see in the preceding three figures that the most leverage regarding the wavelength dependence of the opacity, and hence of τ_*, comes at the shortest wavelengths, below the Ne K-shell edges near 13 Å. The Fe and Ne edges and the low O abundance conspire to make the opacity rather flatter than the generally expected $\kappa \propto \lambda^3$ relationship seen from individual elements' photoionization cross-sections. Most of the strong lines in the MEG spectra of O stars are between 12 and 18 Å, where the opacity is relatively constant. This demonstrates the need for the use of realistic wind opacity models when interpreting trends in grating spectra of O stars and explains why the wavelength trend of τ_* values was not noted in the initial studies.

Furthermore, the paucity of useful emission lines longward of the O K-shell edge makes it difficult to discriminate among various wind opacity models, although in principle, lines longward of this edge could enable us to diagnose the altered CNO-processed abundances with some certainty. And emission lines longward of the N K-shell edge near 26 Å would be especially useful, but there are none in the *Chandra* spectrum. The N VII Lyβ line at 20.910 Å is quite weak and does not provide a strong constraint on τ_*, although it does favour the subsolar metallicity opacity model. The longest wavelength line which we are able to reliably fit is the helium-like O VII complex near 21.8 Å. We fit the resonance and intercombination lines simultaneously (the forbidden line is not present due to 2^3S–2^3P photoexcitation by the photospheric UV field), with the profile parameters τ_* and R_o tied together for the two lines. However, the resonance line in this complex may be subject to resonance scattering (Leutenegger et al. 2007) – it may be optically thick to its own radiation (as distinct from the effects of continuum opacity of the overlying wind that leads to the observed skewness and blueshifts in all of the line profiles). Resonance scattering tends to make broadened, asymmetric and blueshifted lines more symmetric, and thus the τ_* value we derive from fitting this complex may be underestimated. If this is the case, then this line complex too would favour the subsolar metallicity wind opacity model, as shown in Fig. 14. We also note that the only other line of the 16 we analyse that is likely to be optically thick to resonance scattering is the O VII

Lyα line at 18.969 Å, so the τ_* determination for that line may also be somewhat underestimated.

We also can see from a careful inspection of the opacity model that the mass-loss rate determination from fitting a set of τ_* values is mostly sensitive to the cross-section contributions from N, O and Fe. Alterations of O and N abundances due to CNO processing will have only a modest effect on the results, however. The sum of the contributions of N and O (as well as He and C) is what affects the overall opacity level between about 15 and 20 Å, with Fe – and to a lesser extent, Ne – making a significant contribution at shorter wavelengths. This demonstrates that accurate determinations of abundances for O stars are perhaps the biggest factor in enabling the determination of clumping-independent mass-loss rates from high-resolution X-ray spectra. But when fitting a large ensemble of lines that span a relatively wide range of wavelengths, knowing the overall metallicity is probably sufficient, although including a realistic mixture of elements (and thus absorption edges) is important too.

5.2 Sources of uncertainty in the mass-loss rate determination

The uncertainty in the mass-loss rate determination we have found from the fits to the ensemble of τ_* values, derived from fitting the individual line profiles, come from three sources. The first is the formal uncertainty on the mass-loss rate model that stems from the uncertainties on the individual line profile fits (represented by the error bars on the τ_* points in Fig. 13, for example). For the subsolar metallicity opacity model the 68 per cent confidence limit range on the fitted mass-loss rate extends from 3.25 to 3.73 × 10^{-6} M$_\odot$ yr^{-1}, representing an uncertainty of a little less than 10 per cent on the best-fitting value of 3.50×10^{-6} M$_\odot$ yr^{-1}.

The second source of uncertainty arises from our imperfect knowledge of the wind terminal velocity (and, most importantly, the terminal velocity of the X-ray-emitting plasma itself). However, as we have shown (see Fig. 11), the data themselves indicate that our adopted terminal velocity of $v_\infty = 2250$ km s^{-1} is well supported. Three of the lines we show in that figure have best-fitting terminal velocity values near 2350 km s^{-1}, which is also the terminal velocity derived from a careful analysis of the UV line profiles by Haser (1995). When we refit the representative Fe XVII line at 15.014 Å using this higher terminal velocity, we found a reduction in our derived τ_* value of 15 per cent. If this scaling holds for all lines, then using this slightly higher value of the terminal velocity will lead to a downward revision of our derived mass-loss rate of about 15 per cent. (Note that the terminal velocity enters into the denominator of the expression for τ_*, and that will mitigate this adjustment slightly.) Similar considerations pertain to our assumption about the wind velocity parameter, β.

The third, and largest, source of uncertainty is due to the abundances. We estimate that the abundances derived for ζ Pup from the analysis of UV and optical data have a precision of only about a factor of 2 (Bouret et al., in preparation). However, we note that they are in good agreement with the independent, X-ray-based determination from Zhekov & Palla (2007), providing additional confidence as to their accuracy. We can see from the comparison of the subsolar metallicity model to the solar abundance model that the mass-loss rate varies by about a factor of 2 between these two assumed opacity models, although the solar abundance model is included in our analysis not so much as a realistic alternate model, but simply as a plausible upper bound to the atomic opacity; the subsolar metallicity model is more realistic due to the constraints

on it provided by observations in other wavelength bands (Bouret et al. 2008; Bouret et al., in preparation), and of course, the evolved nature of ζ Pup implies that we should not expect to find solar abundances in its wind. However, the overall CNO metallicity of 0.53 solar is lower than expected, given the uniformly solar abundances in nearby massive stars (Przybilla, Nieva & Butler 2008). Thus, a conservative estimate of the allowed range of the mass-loss rate of ζ Pup derived from the X-ray line profile fitting is roughly 2 to 4 × 10^{-6} M$_\odot$ yr^{-1}, with our best estimate being 3.50×10^{-6} M$_\odot$ yr^{-1}. This mass-loss rate is only a little lower than the maximum mass-loss rate of 4.2×10^{-6} M$_\odot$ yr^{-1} (Puls et al. 2006), implying a small amount of clumping in the outer wind, and a small adjustment to the clumping factor in the inner wind determined by Puls et al. (2006).

Any future modification to the accepted abundances of ζ Pup could lead to a change in the mass-loss rate implied by our X-ray line profile analysis. To a good approximation, such a change would simply involve scaling the X-ray line profile mass-loss rate by the reciprocal of the change in the overall metallicity, for reasons discussed at the end of the previous subsection.

5.3 Location of the X-ray-emitting plasma

The analysis of the 16 lines and line complexes in the *Chandra* spectrum of ζ Pup also enables us to derive values of the onset radius of the wind-shock X-ray emission from the profiles. These results are shown in the lower panel of Fig. 10, and are completely consistent with the expectations of the wind-shock structure induced by the line-driven instability (Feldmeier et al. 1997; Runacres & Owocki 2002). That is, an onset radius of $R_o \approx 1.5R_*$ (from a weighted fit to the results from the 16 fitted lines and line complexes; with an uncertainty of $0.1R_*$). We have searched for a trend with wavelength in these values and found none.[7] Thus, the simplest interpretation is that there is a universal radius of the onset of X-ray emission and it occurs near $1.5R_*$ (half a stellar radius above the photosphere). This result had already been noted by Kramer et al. (2003), though we show it more robustly here. This same result can also be seen in the late O supergiant ζ Ori (Cohen et al. 2006). And this result is also consistent with the joint analysis of X-ray line profile shapes and helium-like forbidden-to-intercombination line ratios for four O stars as described by Leutenegger et al. (2006).

5.4 Comparison with previous analyses

Finally, let us consider why we have found a trend in wavelength for the fiducial optical depth values, τ_*, derived from the same *Chandra* data that led Kramer et al. (2003) to report that there was no obvious trend. The two biggest factors leading to this new result are our more careful assessment of line blends, and our inclusion of many weak, but important, lines at short wavelength. Kramer et al. (2003) included only one line shortward of the Ne X Lyα line at 12.134 Å, whereas we report on nine lines or line complexes in this range (including two helium-like complexes, which Kramer et al. (2003) excluded from their analysis). While many of these lines are weak and do not provide very strong constraints when considered individually, taken together, they are highly statistically

---

[7] An unweighted fit of an assumed linear trend shows a modest increase with wavelength, but that result is significant at only the 1σ level, and when we perform a weighted fit – with the weights inversely proportional to the uncertainties on the individual measurements – the significance is less than 1σ.

significant. As for line blends, Kramer et al. (2003) included the N VII Lyα line at 24.781 Å and the Fe XVII complex near 15.26 Å, both of which we have determined are too blended to allow the extraction of reliable information about their intrinsic profile shapes. Furthermore, we properly account for the blended Fe XVII lines at 17.051 and 17.096 Å, fitting them simultaneously, while Kramer et al. (2003) fit them as a single line.

None the less, if we exclude the blended 17.05, 17.10 Å lines, our τ_* values for each line also analysed by Kramer et al. (2003) are in agreement to within the error bars. Similarly, for five un-blended lines in the analysis of the same data by Yamamoto et al. (2007), we find consistent results. In fact, the wavelength trend of τ_* is fully consistent with the τ_* values found by Yamamoto et al. (2007), but there were not enough lines in that study for the trend to be unambiguously detected. The seven additional lines and line complexes that are not analysed in any other study (Kramer et al. 2003; Leutenegger et al. 2006; Yamamoto et al. 2007) but which we analyse here are crucial for mapping out the wavelength dependence of τ_*.

An additional factor that enabled us to determine that the wave-length trend in τ_* is consistent with that expected from the form of the atomic opacity of the wind is our use of a detailed model of the wind opacity. It is relatively flat over much of the wavelength range encompassing the strong lines in the *Chandra* spectrum. Specifi-cally, from about 12 Å to about 18 Å, the presence of successive ionization edges makes the overall opacity roughly flat. Thus, for a trend to be apparent, short-wavelength lines have to be included in the analysis. Previous studies have computed wind X-ray opacities – several based on detailed non-LTE wind modelling – and used them for the analysis of X-ray spectra (Hillier et al. 1993; MacFarlane, Cohen & Wang 1994; Pauldrach et al. 1994; Cohen et al. 1996; Hillier & Miller 1998; Waldron et al. 1998; Pauldrach, Hoffmann & Lennon 2001; Oskinova et al. 2006; Krtička & Kubát 2009). But the present study is the first to demonstrate the importance of the combined effect of multiple edges in flattening the opacity in the middle of the *Chandra* bandpass. And it is the first to explore the sensitivity of the fitting of a high-resolution X-ray spectrum to the assumed wind opacity.

Finally, the mass-loss rate reduction derived here is only a little less than a factor of 3, while earlier analyses suggested that, without porosity, much larger mass-loss rate reductions would be required to explain the only modestly shifted and asymmetric profiles (Kramer et al. 2003; Oskinova et al. 2006). Here too, the wind opacity is the key. The overall opacity of the wind is significantly lower than had been previously assumed, implying that the mass-loss rate reduction is not as great as had been assumed. Again, this is primarily due to the significantly subsolar abundances (especially of oxygen) in ζ Pup.

6 CONCLUSIONS

By quantitatively analysing all the X-ray line profiles in the *Chandra* spectrum, we have determined a mass-loss rate of $3.5 \times 10^{-6} \, \mathrm{M_\odot \, yr^{-1}}$, with a confidence range of 2 to $4 \times 10^{-6} \, \mathrm{M_\odot \, yr^{-1}}$. Within the context of the simple, spherically symmetric wind emis-sion and absorption model we employ, the largest uncertainty arises from the abundances used in the atomic opacity model. This method of mass-loss rate determination from X-ray profiles is a potentially powerful tool for addressing the important issue of the actual mass-loss rates of O stars. Care must be taken in the profile analysis, however, as well as in the interpretation of the trends found in the derived τ_* values. It is especially important to use a realistic model

of the wind opacity. And for O stars with weaker winds, especially, it will be important to verify that the X-ray profiles are consistent with the overall paradigm of embedded wind shocks. Here, an indepen-dent determination of the terminal velocity of the X-ray-emitting plasma by analysing the widths and profiles of the observed X-ray lines themselves will be crucial. In the case of ζ Pup, we have shown that the X-ray profiles are in fact consistent with the same wind kinematics seen in UV absorption-line spectra of the bulk wind. And the profile analysis also strongly constrains the onset radius of X-ray production to be about $r = 1.5R_*$.

An additional conclusion from the profile analysis is that there is no need to invoke large-scale porosity to explain individual line profiles, as the overall wavelength trend is completely consistent (within the measurement errors) with the wavelength dependence of the atomic opacity. The lower-than-expected wind optical depths are simply due to a reduction in the wind mass-loss rate. This modest reduction is consistent with other recent determinations that account for the effect of small-scale clumping on density-squared diagnostics and ionization corrections (Puls et al. 2006).

REFERENCES

Asplund M., Grevesse N., Sauval A. J., 2005, in Bash F. N., Barnes T. G., eds, Cosmic Abundances as Records of Stellar Evolution and Nucle-osynthesis. Astron. Soc. Pac., San Francisco, p. 25
Berghoefer T. W., Baade D., Schmitt J. H. M. M., Kudritzki R.-P., Hillier D. J., Pauldrach A. W. A., 1996, A&A, 306, 899
Bouret J.-C., Lanz T., Hillier D. J., 2005, A&A, 438, 301
Bouret J.-C., Lanz T., Hillier D. J., Foellmi C., 2008, in Hamann W.-R., Feldmeier A., Oskinova L. M., eds, Clumping in Hot Star Winds. Universitatsverlag, Potsdam, p. 31
Canizares C. R. et al., 2005, PASP, 117, 1144
Cash W., 1979, ApJ, 228, 939
Cassinelli J. P., Miller N. A., Waldron W. L., MacFarlane J. J., Cohen D. H., 2001, ApJ, 554, L55
Castor J. I., Abbott D. C., Klein R. I., 1975, ApJ, 195, 157
Cohen D. H., Cooper R. G., MacFarlane J. J., Owocki S. P., Cassinelli J. P., Wang P., 1996, ApJ, 460, 506
Cohen D. H., Leutenegger M. A., Grizzard K. T., Reed C. L., Kramer R. H., Owocki S. P., 2006, MNRAS, 368, 1905
Cohen D. H., Leutenegger M. A., Townsend R. H. D., 2008, in Hamann W.-R., Feldmeier A., Oskinova L. M., eds, Clumping in Hot Star Winds. Universitatsverlag, Potsdam, p. 209
Dessart L., Owocki S. P., 2003, A&A, 406, L1
Eversberg T., Lepine S., Moffat A. F. J., 1998, ApJ, 494, 799

Feldmeier A., Puls J., Pauldrach A. W. A., 1997, A&A, 322, 878
Fullerton A. W., Massa D. L., Prinja R. K., 2006, ApJ, 637, 1025
Glebocki R., Gnacinski P., Stawikowski A., 2000, Acta Astron., 50, 509
Hamann W.-R., Koesterke L., 1999, A&A, 335, 1003
Hamann W.-R., Feldmeier A., Oskinova L. M., 2008, Clumping in Hot Star Winds. Universitatsverlag, Potsdam
Haser S. M., 1995, Universitäts-Sternwarte der Ludwig-Maximillian Universität, München
Hillier D. J., Miller D. L., 1998, ApJ, 496, 407
Hillier D. J., Miller D. L., 1999, ApJ, 519, 354
Hillier D. J., Kudritzki R.-P., Pauldrach A. W. A., Baade D., Cassinelli J. P., Puls J., Schmitt J. H. M. M., 1993, ApJ, 276, 117
Howarth I. D., Prinja R. K., Massa D., 1995, ApJ, 452, L65
Ignace R., 2001, ApJ, 549, 119
Kahn S. M., Leutenegger M. A., Cottam J., Rauw G., Vreux J.-M., den Boggende A. J. F., Mewe R., Güdel M., 2001, A&A, 365, L312
Kramer R. H., Cohen D. H., Owocki S. P., 2003, ApJ, 592, 532
Krtička J., Kubát J., 2009, MNRAS, 394, 2065
Lamers H. J. G. L. M., Leitherer C., 1993, ApJ, 412, 771
Lanz T., Hubeny I., 2003, ApJS, 146, 417
Leutenegger M. A., Paerels F. B. S., Kahn S. M., Cohen D. H., 2006, ApJ, 650, 1096
Leutenegger M. A., Owocki S. P., Paerels F. B. S., Kahn S. M., 2007, ApJ, 659, 642
MacFarlane J. J., Cassinelli J. P., Welsh B. Y., Vedder P. W., Vallerga J. V., Waldron W. L., 1991, ApJ, 380, 564
MacFarlane J. J., Cohen D. H., Wang P., 1994, ApJ, 437, 351
Markova N., Puls J., Repolust T., Markov H., 2004, A&A, 413, 693
Marshall H. L., Dewey D., Ishibashi K., 2004, in Flanagan K. A., Siegmund O. H. W., eds, Proc. SPIE Vol. 5165, X-ray and Gamma-Ray Instrumentation for Astronomy. SPIE, p. 457
Oskinova L., Feldmeier A., Hamann W.-R., 2006, MNRAS, 372, 313
Owocki S. P., Cohen D. H., 2001, ApJ, 559, 1108
Owocki S. P., Cohen D. H., 2006, ApJ, 648, 565
Owocki S. P., Castor J. I., Rybicki G. B., 1988, ApJ, 335, 914

Pauldrach A. W. A., 2003, Rev. Modern Astron., 16, 133
Pauldrach A. W. A., Puls J., Kudritzki R.-P., 1986, A&A, 164, 86
Pauldrach A. W. A., Kudritzki R.-P., Puls J., Butler K., Hunsinger J., 1994, A&A, 283, 525
Pauldrach A. W. A., Hoffmann T. L., Lennon M., 2001, A&A, 375, 161
Perryman M. A. C. et al., 1997, A&A, 323, L49
Press W. H., Flannery B. P., Teukolsky S. A., Vetterling W. T., 2007, Numerical Recipes, 3rd edn. Cambridge Univ. Press, Cambridge
Prinja R. K., Barlow M. J., Howarth I. D., 1990, ApJ, 361, 607
Przybilla N., Nieva M.-F., Butler K., 2008, ApJ, 688, L103
Puls J. et al., 1996, A&A, 305, 171
Puls J., Markova N., Scuderi S., Stanghellini C., Taranova O. G., Burnley A. W., Howarth I. D., 2006, A&A, 454, 625
Puls J., Vink J. S., Najarro F., 2008, A&AR, 16, 209
Repolust T., Puls J., Herrero A., 2004, A&A, 415, 349
Runacres M. C., Owocki S. P., 2002, A&A, 381, 1015
Sahu M. S., 1992, PhD thesis, Univ. Groningen, Groningen
Sahu M., Blaauw A., 1993, in Cassinelli J. P., Churchwell E. B., eds, Massive Stars: Their Lives in the Interstellar Medium. Astron. Soc. Pac., San Francisco, p. 278
Smith R. K., Brickhouse N. S., Liedahl D. A., Raymond J. C., 2001, ApJ, 556, L91
van Leeuwen F., 2007, *Hipparcos*, the New Reduction of the Raw Data. Springer-Verlag, Berlin
Vanbeveren D., de Loore C., van Rensbergen V., 1998, A&AR, 9, 63
Verner D. A., Yakovlev D. G., 1995, A&AS, 109, 125
Waldron W. L., Corcoran M. F., Drake S. A., Smale A. P., 1998, ApJS, 118, 217
Yamamoto N., Takano H., Kitamoto S., Kohmura T., 2007, PASJ, 59, 237
Zhekov S. A., Palla F., 2007, MNRAS, 382, 1124

This paper has been typeset from a TEX/LATEX file prepared by the author.